

## Chapter 6

# Primary Anisotropies

*Trees in the mountains plunder themselves,  
Grease in the flame sizzles itself,  
Cinnamon has a taste, so they hack it down,  
Lacquer has a use, so they strip it off.  
All men know the uses of the useful,  
No man knows the uses of the useless.*

*—Chuang-tzu, 4*

### 6.1 Overview

What can the study of anisotropy tell us about cosmology in general? When the *COBE* DMR team first reported the detection of anisotropies on the  $10^\circ$  scale and larger [153] at the  $10^{-5}$  level, they were widely hailed as the panacea for all cosmological ills and uncertainties. It was quickly realized however that that which makes the discovery so important also makes it less than ideal for pinning down cosmological models: anisotropies at this level are a generic prediction of the gravitational instability picture for structure formation. The *COBE* DMR data *alone* lacks the dynamic range to distinguish between closely related instability scenarios. However, combined with the smaller scale measurements of large scale structure and the CMB itself, its true potential can be tapped.

The CMB suffers from fewer problems of interpretation than large scale structure since fluctuations are likely to be still in the linear regime at last scattering. It therefore has the potential to offer clean tests of the underlying cosmology. The current generation of anisotropy experiments extends the angular scale coverage an order of magnitude down to the degree scale. The next generation of space based experiments will probe yet another

order of magnitude down to the several arcminute scale. It is important to realistically assess what cosmological information lies in the spectrum of anisotropies from arcminute scales on up. The general study of anisotropy formation will be the focus of the remaining portion of this work. In this chapter, we consider primary anisotropy formation. Specifically, we assume that the photons free stream since recombination suffering only gravitational interactions between  $z_* \simeq 1000$  and today. In the next chapter, we will consider processes in the intermediate regime which may alter the anisotropy.

### 6.1.1 Anisotropy Sources

At the most abstract level, there are only two factors relevant to the formation of anisotropies: gravitational interactions and Compton scattering. Nevertheless, their influence encodes a great wealth of cosmological information in the CMB. At the next level of detail, primary anisotropies are characterized by four quantities:

1.  $\Theta_0(\eta_*, \mathbf{x})$ : the intrinsic temperature at last scattering.
2.  $\boldsymbol{\gamma} \cdot [\mathbf{v}_\gamma(\eta_*, \mathbf{x}) - v_{obs}]$ : the line of sight velocity at  $\eta_*$  relative to the observer.
3.  $\partial_x \Psi(\eta, \mathbf{x}(\eta))$ : the gradient of the gravitational potential along the line of sight.
4.  $\partial_\eta \Phi(\eta, \mathbf{x}(\eta))$ : the time derivative of the space curvature along the line of sight.

Obviously intrinsic hot and cold spots on the last scattering surface appear as anisotropies today. The observed temperature of the background is also Doppler shifted due to the line of sight bulk motion (dipole moment) of the photons at last scattering relative to the observer. Our own peculiar velocity will just yield a dipole anisotropy pattern on the sky. The measured dipole in the CMB is almost certainly due to this effect and implies that the local group is moving at  $627 \pm 22$  km/s with respect to the CMB frame [152]. A spatial variation in the photon bulk velocity at last scattering can result in an anisotropy at smaller angles. Gradients in the gravitational potential cause redshifts and blueshifts as the photons climb in and out of potential wells. Changes in the space curvature cause dilation effects due to the implied stretching of space. This effect therefore has the the same origin as the cosmological redshift (see §2.1.2).

Even this description is not very useful unless we specify how the four quantities  $\Theta_0$ ,  $v_\gamma$ ,  $\Psi$  and  $\Phi$  arise. Linear perturbation theory, developed in the last two chapters,

supplies these quantities. Let us summarize those results. The initial conditions and the subsequent evolution of the total matter determines the metric fluctuations  $\Psi$  and  $\Phi$  by the Poisson equation (4.95). These in turn feedback on the matter and radiation through gravitational infall and dilation. For scales outside the horizon, gravitational interactions alone determine the fluctuations and make all particle components in the universe evolve similarly.

Inside the horizon, physical interactions must be taken into account. Before recombination, Compton scattering couples the photons to the baryons. From the Boltzmann equation (4.54) for the multipole moments, this has two significant effects:

1.  $\mathbf{v}_b = \mathbf{v}_\gamma$ : photons and baryons track each other during their evolution.
2.  $\Theta_\ell \propto e^{-\tau}, \ell \geq 2$ : except for the dipole, anisotropies are strongly damped.

Together they imply that the photons are isotropic in the baryon rest frame. This also explains why the photons may be characterized by their temperature and bulk velocity alone.

Since the two velocities are equal, photons and baryons cannot stream away from each other. This means that number density fluctuations are frozen in, *i.e.* the entropy fluctuation is constant [see equation (4.51)]. The photons and baryons therefore evolve adiabatically and may be thought of as a single photon-baryon fluid. Photon pressure resists the gravitational compression of the fluid and sets up acoustic waves. The oscillations are frozen in at last scattering leading to intrinsic temperature fluctuations  $\Theta_0$  from compression and rarefaction as well as bulk motion of the fluid  $v_\gamma$ . At the smallest scales, photon diffusion amongst the baryons and subsequent rescattering collisionally damps fluctuations as  $e^{-\tau}$  leading to a small scale cut off in the spectrum at last scattering.

### 6.1.2 Projection and Free Streaming

After last scattering, photons free stream toward the observer on radial null geodesics and suffer only the gravitational interactions of redshift and dilation. Spatial fluctuations on the last scattering surface are observed as anisotropies in the sky. Free streaming thus transfers  $\ell = 0$  inhomogeneities and  $\ell = 1$  bulk velocities to high multipoles as the  $\ell$ -mode coupling of the Boltzmann equation (4.54) suggests. Microphysically, this occurs because the paths of photons coming from hot and cold regions on the last scattering

surface cross. Isotropic  $\ell = 0$  density perturbations are thus averaged away collisionlessly. It is also evident that this conversion does not occur for superhorizon scales  $k\eta \ll 1$  since the photons can travel only a small fraction of a wavelength.

The background curvature also affects the photons in the free streaming limit. Due to the more rapid deviation of geodesics, a given length scale will correspond to a smaller angle in an open universe than a flat one. Thus the *only* effect of negative spatial curvature during free streaming is to speed the transfer of power to higher multipoles [see equation (4.54)]. Its effect is noticeable if the angular scale  $\theta \sim \ell^{-1}$  is less than the ratio of the physical scale to the curvature radius  $\sqrt{-K}/k$ . Notice that even the lowest eigenmode,  $k = \sqrt{-K}$  possesses  $\ell$ -mode coupling and hence free streaming damping of low-order multipoles, once the horizon becomes larger than the curvature radius  $\eta\sqrt{-K} \gtrsim 1$ . As discussed in §4.1.3, this is simply because the  $k = \sqrt{-K}$  eigenmode has structure only as large as the curvature scale. After the curvature scale passes inside the horizon, structure at this scale is seen as an anisotropy on the sky as opposed to the featureless lowest flat eigenmode  $k = 0$ . If a truly scale invariant spectrum is desired, the modes must be “over-completed” by taking  $k \rightarrow 0$  in the open case as well.

### 6.1.3 Mathematical Description

A full description of the photon temperature must be two dimensional to account for both the spatial and angular distribution  $\Theta(\eta, \mathbf{x}, \boldsymbol{\gamma})$ . However, we can only observe the CMB from one location and hence have information on the angular distribution alone. The ensemble average of the angular temperature correlation function can be decomposed into the moments of the normal modes as

$$\langle \Theta^*(\eta, \mathbf{x}, \boldsymbol{\gamma}) \Theta(\eta, \mathbf{x}, \boldsymbol{\gamma}') \rangle = \frac{V}{2\pi^2} \int_{k \geq \sqrt{-K}}^{\infty} \sum_{\ell} \frac{1}{2\ell + 1} k^3 |\Theta_{\ell}(\eta, k)|^2 P_{\ell}(\boldsymbol{\gamma}' \cdot \boldsymbol{\gamma}), \quad (6.1)$$

where  $P_{\ell}$  is a Legendre polynomial. Orthogonality of the  $P_{\ell}$ 's insures that  $\ell$  modes do not couple and the random phase assumption does the same for the  $k$  modes. For models which predict supercurvature fluctuations, the lower limit of the integral should be taken to zero. The power in the  $\ell$ th multipole is usually denoted  $C_{\ell}$ , where

$$\frac{2\ell + 1}{4\pi} C_{\ell} = \frac{V}{2\pi^2} \int_{k \geq \sqrt{-K}}^{\infty} \frac{dk}{k} k^3 \frac{|\Theta_{\ell}(\eta, k)|^2}{2\ell + 1}. \quad (6.2)$$

Note that the ensemble average anisotropy predicted for an experiment with window function  $W_\ell$  is  $(\Delta T/T)^2 = \sum (2\ell + 1)W_\ell C_\ell / 4\pi$  with  $C_\ell$  evaluated at the present.<sup>1</sup> We can also sum in  $\ell$  to obtain

$$|\Theta + \Psi|_{rms}^2 \equiv |\Theta_0 + \Psi|^2 + \sum_{\ell=1}^{\infty} \frac{|\Theta_\ell|^2}{2\ell + 1}, \quad (6.3)$$

which measures the total power in a single  $k$ -mode. Since fluctuations are merely transferred to high multipoles by free streaming, the rms is conserved if  $\dot{\Phi} = \dot{\Psi} = \dot{\tau} = 0$ , as is evident from equation (4.52). This merely indicates that the blueshift from falling into a static potential is exactly cancelled by the redshift climbing out.

Up until this point, the initial spectrum in  $k$  has been left arbitrary since  $k$  modes evolve independently. It is always possible to incorporate the evolution as a transfer function in  $k$ . However, each multipole  $\ell$  of  $C_\ell$  contains a sum over modes and does not evolve independently. We will often employ as examples simple power law initial spectra for which  $\mathcal{P}(k) = k^3 |\Phi(0, k)|^2 \propto k^{n-1}$  and  $k^3 |S(0, k)|^2 \propto k^{m+3}$  for adiabatic and isocurvature modes respectively. Thus  $n = 1$  and  $m = -3$  are the scale invariant choices for the spectrum. Here scale invariance represents equal power per logarithmic  $k$  interval and is not equivalent to the commonly employed choice of equal power per logarithmic  $\tilde{k} = (k^2 + K)^{1/2}$  interval (see §4.1.1 and Appendix B.4).

It is often instructive to consider the full angular and spatial information contained in the two dimensional transfer function

$$T_\ell^2(k) \mathcal{P}(k) \equiv \frac{V}{2\pi^2} \frac{1}{2\ell + 1} k^3 |\Theta_\ell|^2. \quad (6.4)$$

which satisfies  $(2\ell + 1)C_\ell / 4\pi = \int T_\ell^2(k) \mathcal{P}(k) d \ln k$  for any initial spectra. Note that  $\ell T_\ell^2$  also represents the power per logarithmic interval in  $k$  and  $\ell$  of anisotropies in the scale invariant model.

## 6.2 Sachs-Wolfe Effect

On large scales, gravity dominates the anisotropy through redshift and dilation [138]. Its effects are usually broken up into two parts. Contributions at or before last scattering combine to form the ordinary Sachs-Wolfe (SW) effect. Those occurring after last

---

<sup>1</sup>We only observe one realization of the ensemble and thus  $C_\ell$  must be estimated with  $2\ell + 1$  measurements. Reversing this statement, there is a ‘‘cosmic variance,’’ associated with a  $\chi^2$  distribution of  $2\ell + 1$  degrees of freedom, in the theoretical predictions for even an ideal measurement.

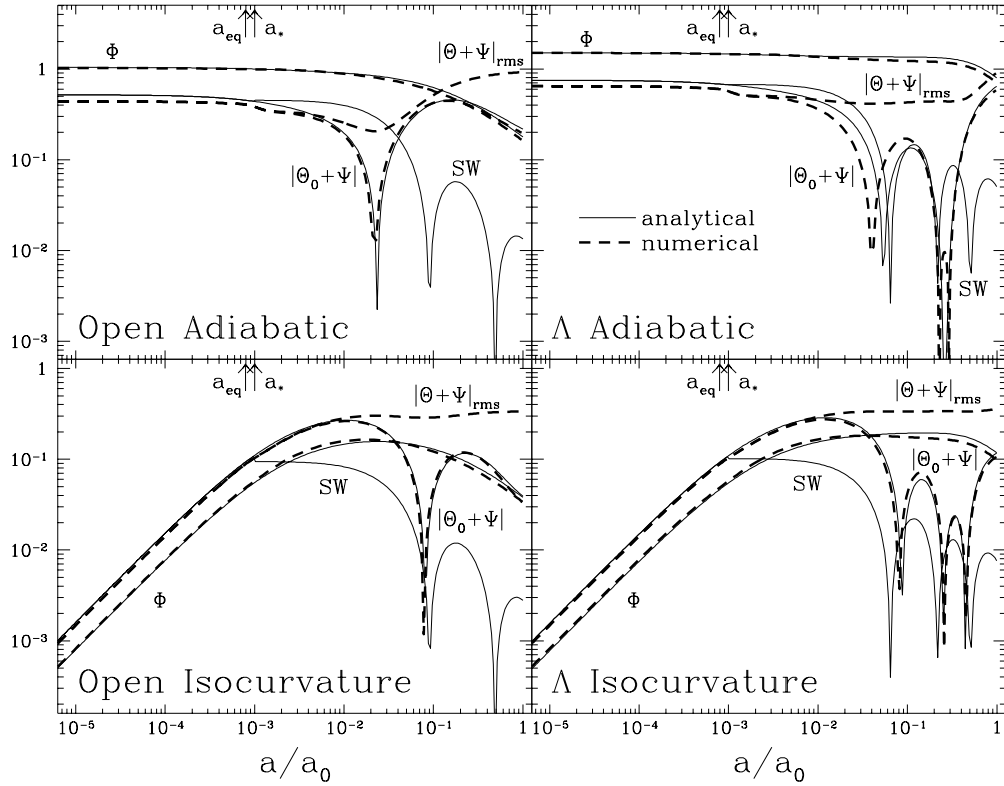


Figure 6.1: Sachs-Wolfe Evolution

In the adiabatic case, temperature fluctuations are enhanced in gravitational wells such that  $\Theta_0$  and  $\Psi$  cancel, yielding  $\Theta_0 + \Psi = \Psi/3$  in the matter dominated epoch. For the isocurvature case, the dilation effect creates a net total of  $\Theta_0 + \Psi = 2\Psi$  reflecting the anticorrelated nature of radiation and total density fluctuations. After last scattering at  $a_*$ , this SW contribution (analytic only) collisionlessly damps from the monopole and transfers power to anisotropies. The rms temperature fluctuations (numerical only) acquires contributions after  $a_*$  from the ISW effect due to the radiation (early) and curvature or  $\Lambda$  (late) contributions. The scale here is chosen to be  $k = 4 \times 10^{-4} \text{Mpc}^{-1}$  in an  $\Omega_0 = 0.1$   $h = 0.5$  universe.

scattering are referred to as the integrated Sachs-Wolfe (ISW) effect. After first describing their general nature, we will examine in detail their manifestation in a critical, open and  $\Lambda$ -dominated, adiabatic or isocurvature model.

### 6.2.1 Ordinary Sachs-Wolfe Effect

As the photons climb out of potential wells at last scattering, gravity redshifts the temperature to  $\Theta_0 \rightarrow \Theta_0 + \Psi$ , where  $|\Psi| < 0$  in a potential well. The effective perturbation at last scattering is thus  $[\Theta + \Psi](\eta_*)$ . The combination of intrinsic temperature fluctuations and gravitational redshift is called the ordinary Sachs-Wolfe (SW) effect [138]. For a gauge choice other than Newtonian, the two may be divided up in different ways.

The intrinsic fluctuations at  $\eta_*$  are in turn determined by gravitational effects *before* last scattering. If  $k\eta \ll 1$ , the Boltzmann equation (4.54) reduces to the dilation effect

$$\dot{\Theta}_0 = -\dot{\Phi} \simeq \dot{\Psi}, \quad (6.5)$$

or

$$[\Theta_0 + \Psi](\eta) \simeq \Theta_0(0) + 2\Psi(\eta_*) - \Psi(0). \quad (6.6)$$

Here we have again assumed  $\Pi_T = 0$ , which causes a  $\sim 10\%$  error (see §A.1.1).

### Isocurvature and Adiabatic Cases

Since the isocurvature initial conditions satisfy  $\Psi(0) = 0 = \Theta_0(0)$ , equation (6.5) implies  $\Theta_0(\eta) = \Psi(\eta)$ . The effective superhorizon scale temperature perturbation for isocurvature fluctuations is therefore

$$\Theta_0 + \Psi = 2\Psi. \quad (\text{iso}) \quad (6.7)$$

The growing potential stretches space so as to dilute the photon density in the well. Gravitational redshift out of the well subsequently doubles the effect. Note however that in a low  $\Omega_0 h^2$  model with standard recombination, the potential may not reach its full matter-dominated value of  $\Psi = -\frac{1}{5}S(0)$  from equation (5.38) by last scattering (see Fig. 6.1).

For adiabatic perturbations, the initial conditions require  $\Theta_0(0) = -\frac{1}{2}\Psi(0)$  [see equation (5.21)], reflecting the fact that the photons are overdense inside the potential well [see equation (5.31)]. Although the potential is constant in both the matter- and radiation-dominated epoch, it changes to  $\Psi(a) = \frac{9}{10}\Psi(0)$  through equality. The dilation

effect then brings the photon temperature perturbation in the matter-dominated epoch to  $\Theta(\eta) = -\frac{2}{3}\Psi(\eta)$ . Thus the effective perturbation is

$$[\Theta_0 + \Psi] = \begin{cases} \frac{1}{2}\Psi & \text{RD} \\ \frac{1}{3}\Psi, & \text{MD} \end{cases} \quad (\text{adi}) \quad (6.8)$$

where the latter is the familiar Sachs-Wolfe result. Again since last scattering may occur before full matter domination, one should employ the full form of equation (6.6) instead of the asymptotic form from equations (5.38) and (6.8). After  $a_*$ , the photons climb out of the potential wells, leaving the quantity  $[\Theta_0 + \Psi](\eta_*)$  to be viewed as temperature fluctuations on the sky today.

### Free Streaming Solution

To determine the exact nature of the resultant anisotropies, one must follow the photons from last scattering to the present. The collisionless Boltzmann equation for  $(\Theta + \Psi)/(2\ell + 1)$  takes the same form as the recursion relation for the radial eigenfunctions of the Laplacian [*c.f.* equations (4.13) and (4.54)]. This is natural since the radiation free streams on null geodesics. Thus the spatial fluctuation represented by  $[\Theta + \Psi](\eta_*, k)$  is seen by the distant observer as an anisotropy of

$$\frac{\Theta_\ell(\eta, k)}{2\ell + 1} = [\Theta_0 + \Psi](\eta_*, k) X_\nu^\ell(\chi - \chi_*), \quad (6.9)$$

where recall that  $\chi = \sqrt{-K}\eta$ . In the flat case,  $X_\nu^\ell \rightarrow j_\ell$  which peaks at  $\ell \simeq k(\eta - \eta_*)$ . If the distance traveled by the photon is under a wavelength, *i.e.*  $k(\eta - \eta_*) \ll 1$ , then only  $j_0$  has weight and fluctuations remain in the monopole. As time progresses, power is transferred from the monopole to high  $\ell$  as one would expect from the projection effect (see Fig. 6.1).

In the adiabatic flat case, power law models for the initial conditions  $k^3|\Phi(0)|^2 = Bk^{n-1}$  have a simple form for the Sachs-Wolfe contribution to  $C_\ell$ . If we assume that the universe was matter dominated at last scattering,  $\Theta_0 + \Psi = \frac{1}{3}\Psi$ . From equation (6.2),

$$\begin{aligned} C_\ell^{SW} &\simeq \left(\frac{1}{3} \frac{\Psi(\eta_*)}{\Phi(0)}\right)^2 \frac{2}{\pi} BV \int \frac{dk}{k} k^{n-1} j_\ell^2(k\eta_0) \\ &\simeq \frac{9}{200\sqrt{\pi}} BV \eta_0^{1-n} \frac{\Gamma[(3-n)/2]\Gamma[\ell + (n-1)/2]}{\Gamma[(4-n)/2]\Gamma[\ell + (5-n)/2]}, \end{aligned} \quad (6.10)$$

where we have employed the relation  $\Psi(\eta_*)/\Phi(0) = -9/10$  of equation (5.29). In this flat model,

$$\eta_0 \simeq 2(\Omega_0 H_0^2)^{-1/2} (1 + \ln \Omega_0^{0.085}), \quad (6.11)$$

where the small logarithmic correction is from the rapid expansion at the present in a  $\Lambda$  universe. Notice that for scale invariant spectra, the projection factor  $\eta_0^{n-1}$  vanishes. With equal power at all scales, it does not matter which physical scale gets mapped onto a given angular scale.

Equation (6.10) is more commonly expressed in terms of the amplitude of the matter power spectrum today  $|\Delta_T(\eta_0, k)|^2 = Ak^n$ . From equation (5.27), the relation between the two normalizations is

$$\begin{aligned} B &= \frac{25}{36} k_{eq}^4 D^{-2} A \\ &= \frac{25}{9} (\Omega_0 H_0^2)^2 (a_0/D_0)^2 A, \end{aligned} \quad (6.12)$$

where  $D_0 = D(\eta_0)$  and recall that  $D$  is the pressureless growth factor normalized at equality. Since in a  $\Lambda$  universe, growth is suppressed and  $a_0/D_0 < 1$ , the same matter power spectrum normalization  $A$  implies a greater Sachs-Wolfe anisotropy since it was generated when the potentials were larger. The final expression becomes

$$C_\ell^{SW} \simeq \frac{1}{8\sqrt{\pi}} AV H_0^4 \Omega_0^2 (a_0/D_0)^2 \eta_0^{1-n} \frac{\Gamma[(3-n)/2] \Gamma[\ell + (n-1)/2]}{\Gamma[(4-n)/2] \Gamma[\ell + (5-n)/2]}. \quad (6.13)$$

The factor  $\Omega_0^2 (a_0/D_0)^2 \simeq \Omega_0^{1.54}$  for  $\Lambda$  models [52]. Since  $\Gamma(\ell+2)/\Gamma(\ell) = \ell(\ell+1)$ , the Sachs-Wolfe contribution for a scale invariant  $n=1$  spectrum is flat in  $\ell(\ell+1)C_\ell$ . We will therefore occasionally plot  $\ell(\ell+1)C_\ell/2\pi$  instead of the logarithmic power  $\ell(2\ell+1)C_\ell/4\pi$  as has become standard convention. For  $\ell \gg 1$ , the two conventions yield identical results. Note that this formula describes only the Sachs-Wolfe contributions and does not account for the early ISW and acoustic contributions, which push the high  $\ell$  tail up, and the late ISW effect, which enhances the low  $\ell$  multipoles.

### 6.2.2 Integrated Sachs-Wolfe Effect

If the potentials vary with time, the photon will experience differential redshifts due to the gradient of  $\Psi$ , which no longer yield equal and opposite contributions as the photons enter and exit the potential well, and time dilation from  $\Phi$ . They act like an impulse  $(\dot{\Psi} - \dot{\Phi})\delta\eta$  at some intermediate time  $\eta$  which then free streams to the present. The sum of these contributions along the line of sight is called the integrated Sachs-Wolfe (ISW) effect. By the same reasoning that lead to the solution for the Sachs-Wolfe effect, one can

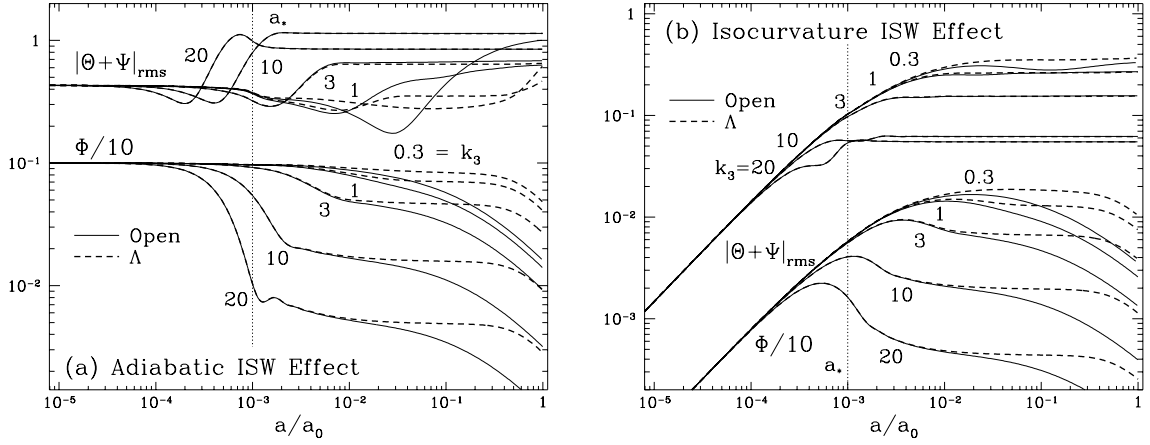


Figure 6.2: ISW Effect

(a) Adiabatic models. Potential decay at horizon crossing during radiation domination boosts scales approaching the first acoustic oscillation through the early ISW effect. Larger scales suffer only the late ISW effects due to the rapid expansion in open and  $\Lambda$  models, leaving a deficit at intermediate scales. (b) Isocurvature models. For small scales, potential growth halts after horizon crossing in the radiation dominated epoch leading to a relative boost for large scale fluctuations. Since this early ISW effect dominates, there is little distinction between open and  $\Lambda$  models. All models have  $\Omega_0 = 0.1, h = 0.5$  with standard recombination and  $k = k_3 \times 10^{-3} \text{Mpc}^{-1}$ .

immediately write down the solution for the combined effect:

$$\frac{\Theta_\ell(\eta, k)}{2\ell + 1} = [\Theta_0 + \Psi](\eta_*, k) X_\nu^\ell(\chi - \chi_*) + \int_{\eta_*}^{\eta} [\dot{\Psi} - \dot{\Phi}](\eta', k) X_\nu^\ell(\chi - \chi') d\eta'. \quad (6.14)$$

Since the potentials for both the adiabatic and isocurvature modes are constant in the matter-dominated epoch, the ISW contribution is separated into two parts:

1. The early ISW effect from radiation domination: (a) isocurvature growth before horizon crossing and (b) pressure growth suppression after horizon crossing for either mode.
2. The late ISW effect due to expansion growth suppression in the  $\Lambda$ - or curvature-dominated epoch.

In adiabatic models, scales which cross the sound horizon in the radiation-dominated epoch experience a boost from the decay of the potential (see Fig. 6.2a). Since the effect is due to radiation pressure and depends only on the epoch of equality, open and  $\Lambda$  models predict identical contributions. These scales will furthermore not experience significant late ISW effects since the potential has already decayed by  $\Lambda$  or curvature domination. On the other

hand, larger scales are unaffected by the early ISW effect and suffer only the consequences of the late ISW effect. Because  $\Lambda$  domination occurs only recently if  $\Omega_0 \gtrsim 0.1$ , the potential will not have had a chance to fully decay and the net effect is smaller than in the corresponding open case.

For isocurvature models, potential growth outside the sound horizon in the radiation-dominated epoch forces the temperature fluctuation to grow with it through the dilation effect (see Fig. 6.2b). Modes which cross only after matter domination experience the full effect of growth. For scales that cross during radiation domination, radiation pressure suppresses further growth. Thus large scale modes are enhanced over small scale modes. Since isocurvature models are dominated by this early ISW effect, the difference between open and  $\Lambda$  models is smaller than in adiabatic models.

The total Sachs-Wolfe effect predicts rich structure in the anisotropy spectra. To understand the full Sachs-Wolfe spectrum, it is necessary to examine simultaneously the spatial and angular information in the radiation. It will therefore be instructive to consider the radiation transfer function  $T_\ell(k)$ , rather than  $C_\ell$  for any one model. Note that  $\ell T_\ell^2(k)$  is equivalent to the logarithmic contribution in  $k$  and  $\ell$  to the anisotropy of a scale invariant model [see equation (6.4)]. Summing in  $k$  produces  $\ell(2\ell + 1)C_\ell/4\pi$  and in  $\ell$  yields  $k^3|\Theta + \Psi|_{rms}^2$  for this model.

### 6.2.3 Adiabatic $\Omega_0 = 1$ models

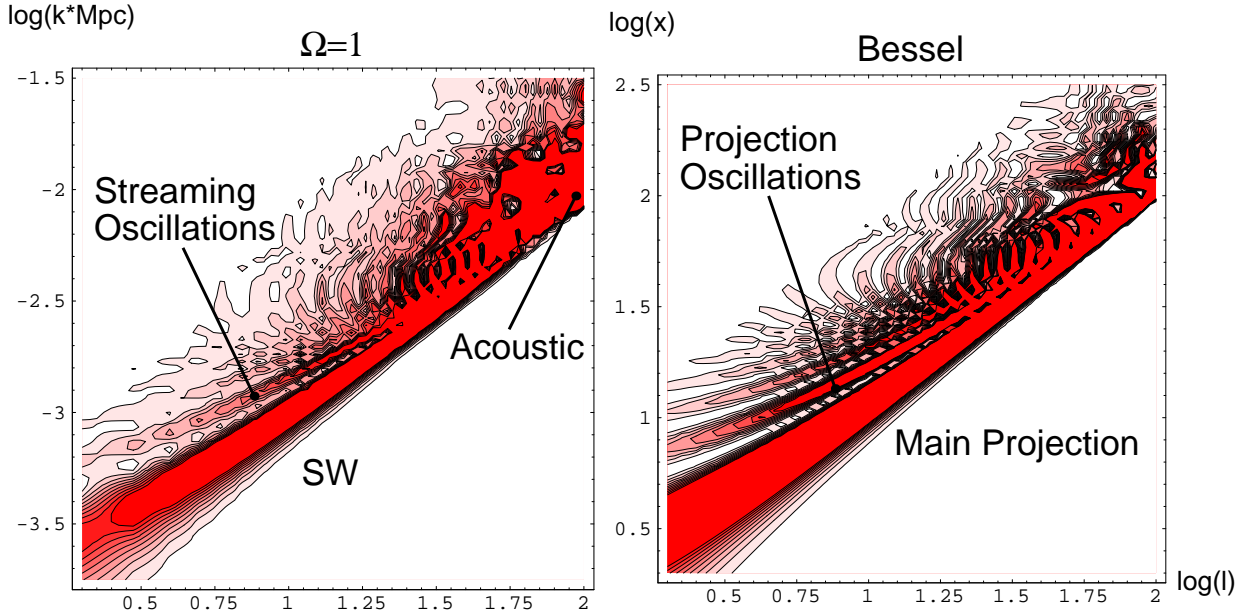
To build intuition for equation (6.14), let us first consider the familiar adiabatic  $\Omega_0 = 1$  model in which the ISW term represents only a small correction. A given  $k$ -mode contributes maximally to the angle that scale subtends on the sky at last scattering. The transfer function therefore displays a sharp ridge corresponding to this correlation (see Fig. 6.3a),

$$\ell_{main} + \frac{1}{2} \simeq kr_\theta(\eta_*), \quad (6.15)$$

where the comoving angular diameter distance is

$$r_\theta(\eta) = (-K)^{-1/2} \sinh(\chi_0 - \chi), \quad (6.16)$$

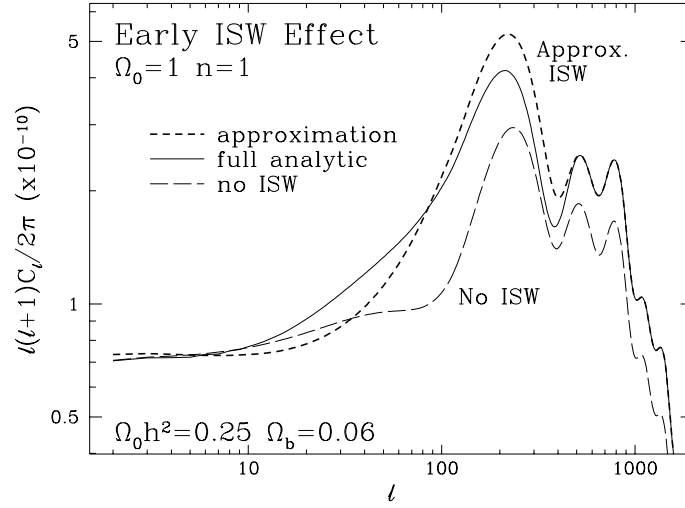
and reduces to  $r_\theta = \eta_0 - \eta_*$  as  $K \rightarrow 0$ . It is evident from Fig. 6.3a that the full result contains more than just this main correlation ridge. The conversion of fluctuations in a spatial eigenmode  $k$  on the last scattering surface into anisotropies on the sky is basically a

Figure 6.3:  $\Omega_0 = 1$  Radiation Transfer Function

Shown here and in Figs. 6.5, 6.8, and 6.10 is the weighted squared transfer function  $\ell T_\ell^2(k)$  which also represents the anisotropy contribution per logarithmic  $k$  and  $\ell$  interval in a scale invariant model. Contours are equally spaced up to a cut off set to best display the features. The strong correlation between  $\ell$  and  $k$  merely reflects the projection of a scale on the last scattering surface to an angle on the sky. At  $\log \ell \gtrsim 2$ , SW contributions fall off and are replaced by the acoustic peaks (saturated here). The detailed structure can be traced to the radial eigenfunction  $X_\nu^\ell(\chi) = j_\ell(x)$  which governs the projection and free streaming oscillations.

projection of the eigenmode in the spherical geometry. For example, a plane wave  $\exp(ik\Delta\eta)$  can be written as a sum over  $j_\ell(k\Delta\eta)Y_\ell^m$ . Since the projection is not precisely one-to-one, a given mode will project onto a range of angles. In fact, it will alias angles equal to and larger than what the main face on  $\mathbf{k} \perp \boldsymbol{\gamma}$  projection of equation (6.15) predicts, *i.e.*  $\ell \leq \ell_{\text{main}}$ , as is clear from Fig. 1.7. This is expressed by the oscillatory structure of the radial eigenfunction. Comparing panels in Fig. 6.3, we see that the structure in the transfer function is indeed due to this effect.

Even with  $\Omega_0 = 1$ , a low  $h \simeq 0.5$  model has additional contributions after last scattering. The early ISW effect affects modes that cross the sound horizon between last scattering and full matter domination. Since these contributions come from near last scat-

Figure 6.4:  $\Omega_0 = 1$  Early ISW Spectrum

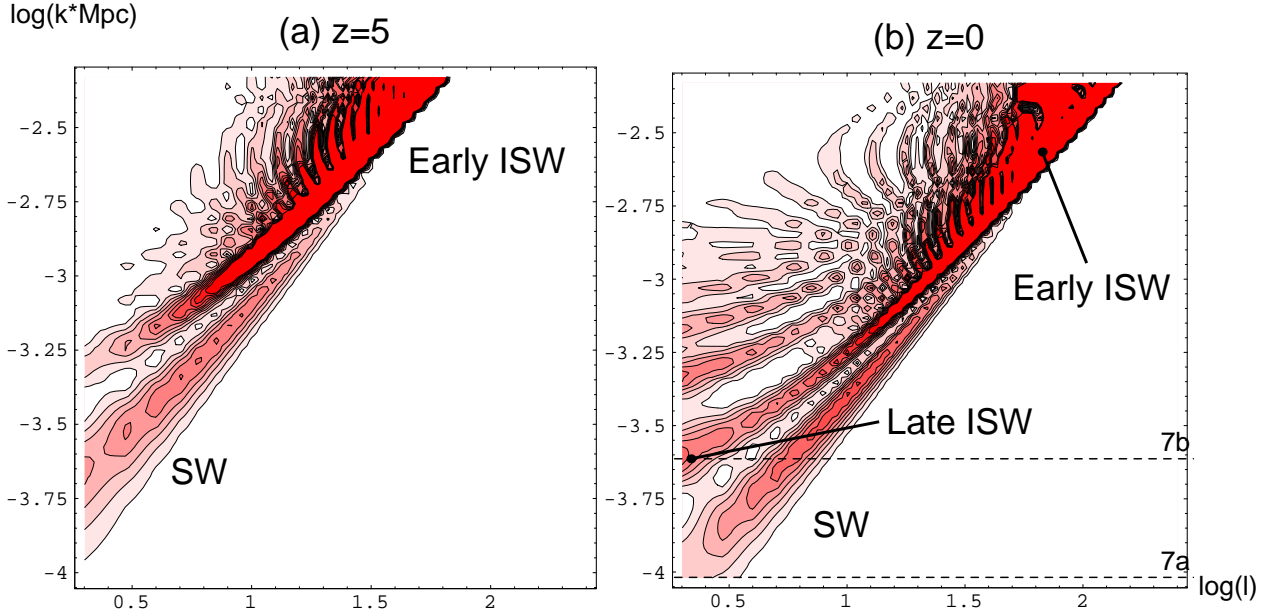
Even in an  $\Omega_0 = 1$   $\Omega_0 h^2 = 0.25$  high matter content universe, early ISW contributions from radiation pressure are non-negligible. Ignoring the ISW effect entirely leads to a significant error in both the large scale normalization and shape of the anisotropies. Approximating *all* of the ISW contribution to occur near recombination through equation (6.17) leads to 10–15% errors in temperature since it comes from more recent times where the fluctuation subtends a larger angle on the sky. The full integration therefore has more power at larger angular scales and makes the rise to the first Doppler peak more gradual. These are analytic results from Appendix A.2.2.

tering, the ISW integral (6.14) may be approximated as

$$\begin{aligned} \int_{\eta_*}^{\eta_0} [\dot{\Psi} - \dot{\Phi}] j_\ell(k(\eta_0 - \eta)) d\eta &\simeq \int_{\eta_*}^{\eta_0} [\dot{\Psi} - \dot{\Phi}] j_\ell(k\eta_0) d\eta \\ &= [\Delta\Psi - \Delta\Phi] j_\ell(k\eta_0), \end{aligned} \quad (6.17)$$

which is strictly only valid for contributions from  $k\eta \ll 1$ . Contributions to the  $k$ th mode in fact occur near horizon crossing where  $k\eta \simeq 1$ . Nevertheless this approximation is instructive.

The early ISW effect adds nearly coherently with the SW effect and in fact cancels it by removing the redshift that the photon would otherwise suffer. At large scales, this brings the total effect down to the matter-dominated  $\frac{1}{3}\Psi(\eta_0)$  value and thus changes the large scale normalization. At scales approaching the sound horizon at last scattering, it increases the effective temperature from the acoustic compression again by removing the cancelling redshift. In Fig. 6.4, we compare the approximation of equation (6.17) to the the full integral and the effect of dropping the contribution entirely. Notice that, aside from its affect on the normalization, the early ISW contribution fills in scales somewhat larger

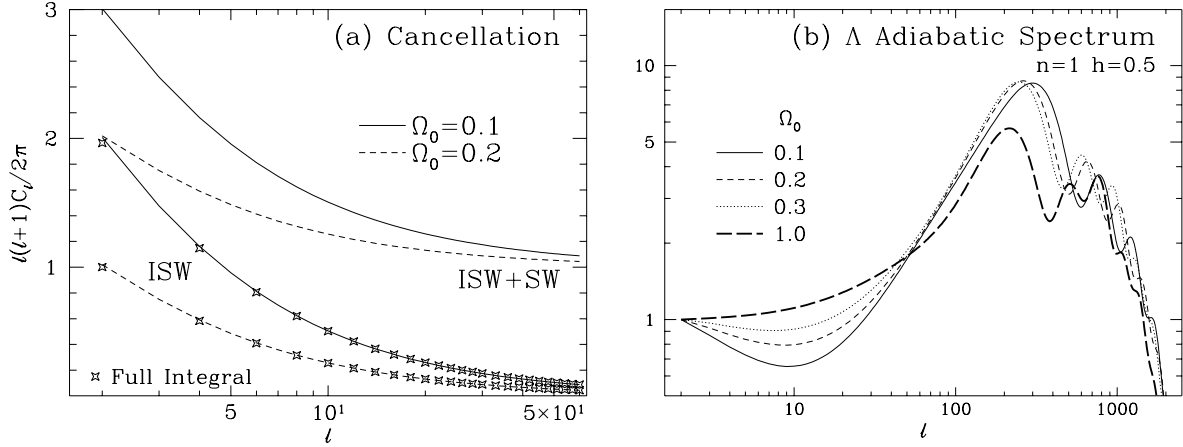
Figure 6.5:  $\Lambda$  Adiabatic Radiation Transfer Function

Unlike the  $\Omega_0 = 1$  case, this scenario has strong contributions after last scattering from the early and late ISW effect. (a) The early ISW effect projects onto a second ridge which is more prominent than the SW ridge at intermediate but not large angles. (b) After  $\Lambda$  domination, the late ISW contributions come free streaming in from the monopole yielding a boost in the low order multipoles for a small range in  $k$ , due to cancellation with SW contributions at the largest scales and crest-trough cancellation at smaller scales. Scales depicted in Fig. 6.7 are marked here by dashed lines. The model here is  $\Omega_0 = 0.1, h = 0.5$  with standard recombination.

than the sound horizon at last scattering. The approximation underestimates the angular scale somewhat by assuming that the contribution comes from the further distance  $\eta_0$  as opposed to the true distance  $\eta_0 - \eta$ .

#### 6.2.4 Adiabatic $\Lambda$ Models

Now let us move onto the more complicated  $\Lambda$  case. For  $\Lambda$  models, the ISW term in equation (6.14) yields both early and late type contributions. The boost on intermediate scales from the early ISW effect is much more dramatic than for the high  $\Omega_0 h^2$  models. In the transfer function, this appears as a high ridge crossing larger angles for the same  $k$  as the SW effect, due to its origin closer to the observer. The maximum contribution the early ISW effect can make is if the potential decayed to zero between last scattering and the present. From the relation  $\dot{\Theta}_0 = -\dot{\Phi}$ , this would yield  $\Theta_0(\eta) = \Theta_0(0) + \Phi(0) = \frac{3}{2}\Phi(0)$ .


 Figure 6.6:  $\Lambda$  Late ISW Spectrum

(a) Analytic Separation. The late ISW effect is cancelled as photons stream through many wavelengths of the perturbation during the decay. The comparison here of the full late ISW integral to the cancellation approximation shows that even at the largest angles, the late ISW contributions are well inside the cancellation regime. The SW effect on the other hand is flat in this representation. As  $\Lambda$  increases, the contribution of the late ISW effect relative to the SW effect increases at low multipoles and appears as a boost. (b) Numerical results. The early ISW effect contributes significantly at scales not much smaller than the cancellation tail of the late ISW effect bending the spectrum back up.

Compared with the matter-dominated SW tail of  $\frac{1}{3}\Psi = -\frac{3}{10}\Phi(0)$ , the early ISW effect can approach a height 5 times greater than the SW tail. Note that the same decay drives the acoustic oscillation to a similar height so that this effect will join smoothly onto the acoustic peaks as we shall see below. The lack of potential decay for scales that enter the horizon during matter domination makes the early ISW ridge drop off at large scales (see Fig. 6.5).

After  $\Lambda$  domination  $a_\Lambda/a_0 = (\Omega_0/\Omega_\Lambda)^{1/3}$ , the potential once again decays. For typical values of  $\Omega_0 \gtrsim 0.1$ , this occurs only recently. Furthermore, the potential at all scales decays at the same rate. The expansion time scale at  $\Lambda$  domination  $\eta_\Lambda = \eta(a_\Lambda)$  sets a critical wavelength corresponding to  $k\eta_\Lambda = 1$ . The ISW integral takes on different form in the two regimes separated by this division

$$\int_{\eta_*}^{\eta_0} [\dot{\Psi} - \dot{\Phi}] j_\ell[k(\eta_0 - \eta)] d\eta \simeq \begin{cases} [\Delta\Psi - \Delta\Phi] j_\ell[(k\eta_0 - k\eta_\Lambda)] & k\eta_\Lambda \ll 1 \\ [\dot{\Psi} - \dot{\Phi}](\eta_k) I_\ell/k, & k\eta_\Lambda \gg 1 \end{cases} \quad (6.18)$$

where  $\Delta\Phi$  and  $\Delta\Psi$  are the changes in the potential from the matter-dominated form of (5.29) to the present. We have used the angle-distance relation (6.15) to find the peak of

$j_\ell$  at  $\eta_k = \eta_0 - (\ell + 1/2)/k$ . The integral  $I_\ell$  is given by

$$I_\ell \equiv \int_0^\infty dx j_\ell(x) = \frac{\sqrt{\pi} \Gamma[\frac{1}{2}(\ell + 1)]}{2 \Gamma[\frac{1}{2}(\ell + 2)]}. \quad (6.19)$$

The limits correspond physically to two cases:

1. If the wavelength is much longer than distance a photon can travel during the decay, photons essentially receive an instantaneous kick. The result is similar to the SW and early ISW effects.
2. In the opposite limit, the photon traverses many wavelengths during the decay and suffers alternating red and blueshifts from crests and troughs. The result is a cancellation of contributions.

Since  $\Lambda$  domination occurs near the present, the critical wavelength is approximately the horizon size at present and yields  $\ell = 0$  monopole contributions along the projection ridge. Thus most contributions will come from the cancellation regime if the  $k$  modes are weighted equally. We can verify this by comparing the cancellation approximation with the full integral for the scale invariant model. Fig. 6.6 shows that in this case the cancellation approximation is excellent. Compared with the SW effect which predicts a flat spectrum, the late ISW  $\Lambda$  contributions fall with  $\ell$  due to cancellation. For the more general case of power law initial spectra  $k^3 |\Phi(0, k)|^2 = Bk^{n-1}$ , the total contribution becomes

$$C_\ell^{ISW} \simeq 2 \left(\frac{9}{10}\right)^2 BV \left(\frac{\Gamma[(\ell + 1)/2]}{\Gamma[(\ell + 2)/2]}\right)^2 \int_0^\infty \frac{dk}{k} k^{n-3} \left[\frac{D}{a} \left(\frac{\dot{D}}{D} - \frac{\dot{a}}{a}\right)\right]_{\eta=\eta_k}^2, \quad (6.20)$$

where we have employed equation (5.29) for the potentials and recall that the growth factor  $D$  is normalized such that  $D(a_{eq}) = a_{eq} = 1$ .

Let us take a closer look at the transfer function in Fig. 6.5. For  $k\eta_\Lambda \ll 1$ , cancellation is ineffective and like its early counterpart, the late ISW effect opposes the SW effect. In Fig. 6.7a, we plot the analytic decomposition of contributions to a  $k$ -mode slice corresponding to these large scales. As one can see from equation (6.18), these modes contribute little to  $\ell \geq 2$ , since  $k(\eta_0 - \eta_\Lambda) \ll 1$ . For intermediate scales, the late ISW effect itself is partially cancelled. The ridge structure of Fig. 6.5 at the low multipoles is due to the late ISW effect adding with every other ridge in the SW free streaming oscillation (see Fig. 6.7b). At the smallest scales, those which would ordinarily contribute to higher

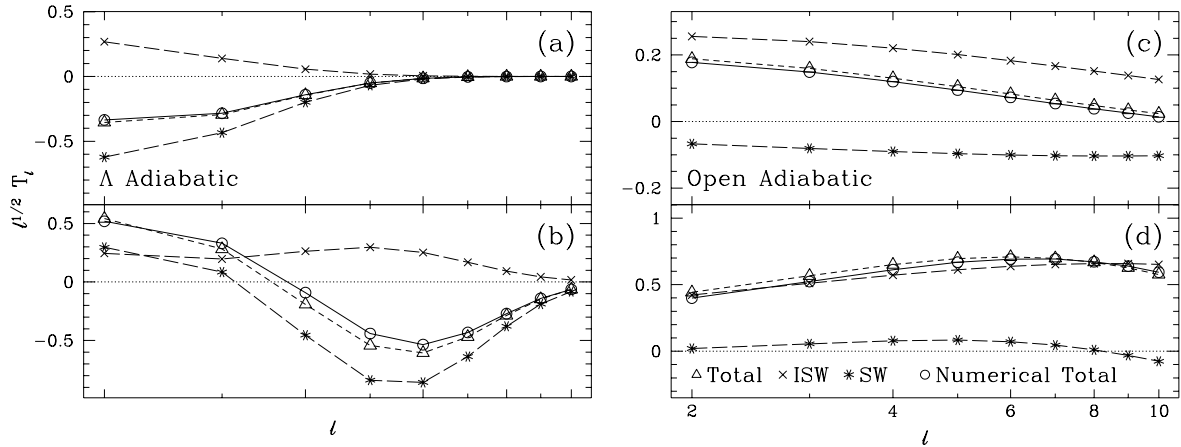


Figure 6.7: Analytic Decomposition: Adiabatic Models

Scales are chosen to match the features in Fig. 6.5 and 6.8.  $\Lambda$  models: (a) At the largest scales, *e.g.* here  $k = 10^{-4} \text{Mpc}^{-1}$ , the SW effect dominates over, but is partially cancelled by, the late ISW effect. (b) Intermediate scale peaks in Fig. 6.5 are due to the late ISW boost of the higher SW projection ridges. Open models: (c) The maximum scale corresponds to the curvature radius  $k = \sqrt{-K}$ . For the SW effect, this scale projects broadly in  $\ell$  peaking near  $\ell \sim 10$ . For the late ISW effect, this scale projects onto the monopole and dipole near curvature domination thus leaving the ISW contributions to decrease smoothly with  $\ell$ . (d) At smaller scales, corresponding to the large ridge in Fig. 6, the late ISW effect projects onto  $\ell \simeq 2 - 10$  and completely dominates leading to a rising spectrum of anisotropies. The models are for  $\Omega_0 = 0.1$   $h = 0.5$  with standard recombination and arbitrary normalization.

order multipoles, the late ISW effect is entirely cancelled. Again this implies that typical adiabatic  $\Lambda$  spectra have a small boost in anisotropies from the late ISW effect only at the lowest multipoles (see Fig. 6.6b).

### 6.2.5 Adiabatic Open Models

Open adiabatic models follow similar physical principles. The early ISW effect depends only on the matter-radiation ratio near last scattering from  $\Omega_0 h^2$  and thus is identical to the  $\Lambda$  case. However, photons curve on their geodesics so that the projection takes the same physical scale to a significantly smaller angular scale. This is quantified by the angle to distance relation (6.16). In the transfer function, one sees that the early ISW ridge is pushed to significantly higher  $\ell$  (see Fig. 6.8).

Curvature dominates at  $a/a_0 = \Omega_0/(1 - \Omega_0)$  leaving the potential more time to decay than in the  $\Lambda$  model. The late ISW effect will therefore be more significant in this model (see Fig. 6.2a). Moreover, the cancellation scale is smaller leading to a less sharp

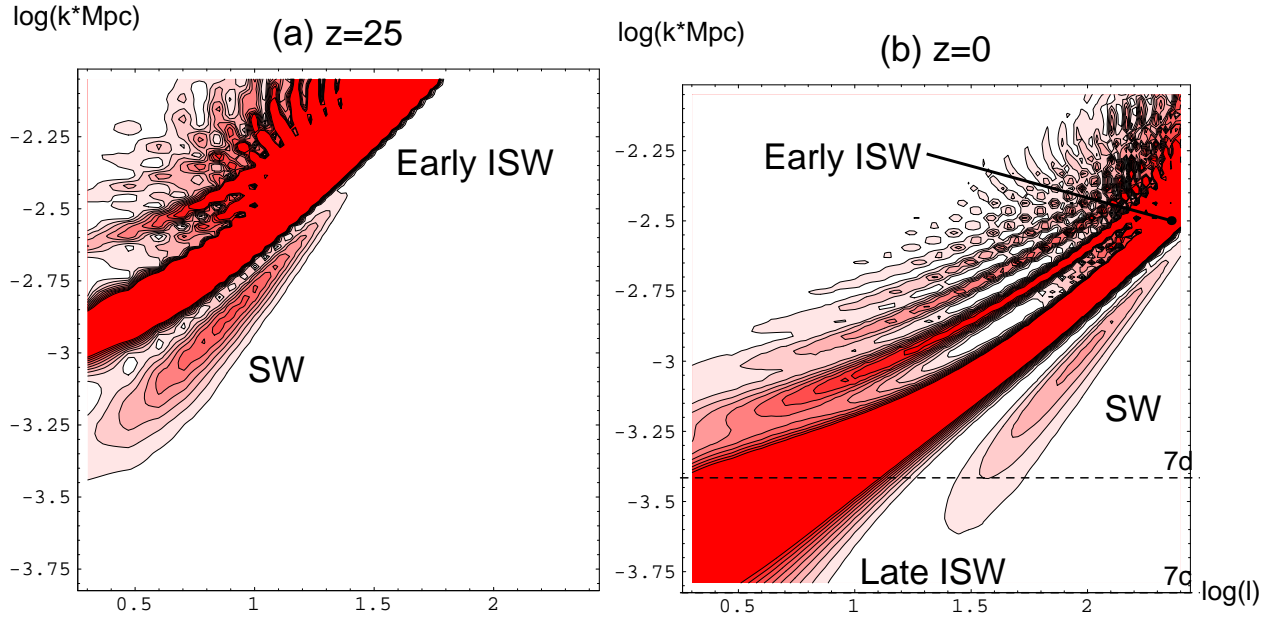


Figure 6.8: Open Adiabatic Radiation Transfer Function

(a) Like the  $\Lambda$  case, the radiation ISW effect contributes significantly to intermediate angle anisotropies. (b) The late ISW effect appearing at the left is much more significant than the corresponding  $\Lambda$  effect. Thus on all angular scales, the total ISW contribution dominates the SW effect. The curvature scale  $\log(k \cdot \text{Mpc}) = -3.8$  intersects the late ISW ridge near the lowest multipoles. Absence of supercurvature contributions can suppress these multipoles. Dashed lines represent scales in Fig. 6.7. The model is  $\Omega_0 = 0.1$ ,  $h = 0.5$ , with standard recombination.

decline with  $k$  (or  $\ell$ ) of the effect. The net result is that the late ISW cancellation tail merges smoothly onto the early ISW rise for sufficiently low  $\Omega_0$ . For  $\Omega_0 \simeq 0.1 - 0.3$ , they overwhelm the SW effect on all scales.

Unlike the flat case, there is a lowest eigenmode corresponding to the curvature scale  $k = \sqrt{-K}$ . Supercurvature scales that would ordinarily contribute to low order multipoles are absent unless the modes are “overcompleted” (see §4.1.3). For the low  $\Omega_0 = 0.1$  example displayed in Fig. 6.8, this cutoff at  $\log(k \cdot \text{Mpc}) \simeq 3.8$  chops off some of the main projection ridge of the late ISW effect for the lowest multipoles. Thus the absence of supercurvature modes in the sum over  $k$  can lead to a slight suppression of the lowest multipoles. With scale invariant weighting of the  $k$ -modes, the spectrum has the form shown in Fig. 6.9. Note that this is the typical [110, 134] but not unique [20] prediction of open inflationary models.

Due to its more recent origin, the late ISW effect projects onto a significantly larger

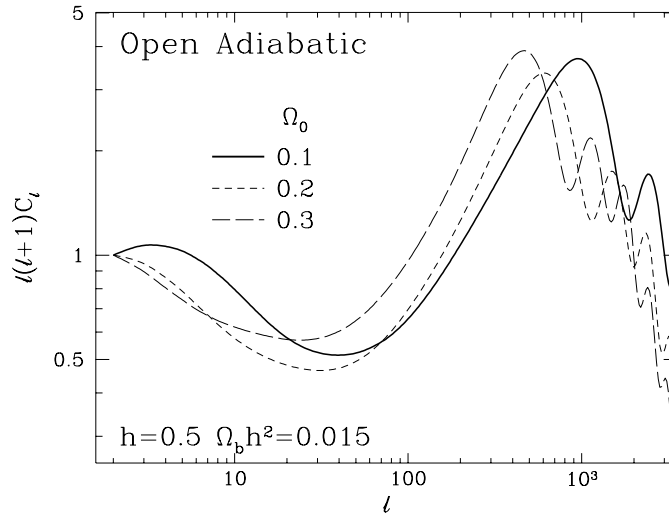


Figure 6.9: Open Adiabatic Spectrum

Scale invariant  $n = 1$  model: equal power per logarithmic  $k$  interval to the curvature scale  $k = \sqrt{-K}$ . The early ISW effect merges with the cancellation tail of the late ISW effect completely dominating the SW contributions. The lack of supercurvature modes can lead to a suppression of low order multipoles as the curvature scale becomes significantly smaller than the horizon (see also Fig. 6.7d). Notice also that geodesic deviation shifts the acoustic contributions more than the early ISW contributions and broaden out the first peak.

angle than the SW effect for a given  $k$ . Examining the individual contributions in Fig. 6.7c, we see that indeed at the curvature scale, the late ISW effect affects the lowest multipoles, whereas the SW effect peaks around  $\ell \simeq 10$ . Thus the presence or lack of supercurvature modes is not as significant as one might naively expect from the fact that the curvature scale subtends  $\ell \simeq 10$  at the horizon distance in an  $\Omega_0 = 0.1$  universe. For a smaller scale chosen to intersect the main late ISW projection ridge in Fig. 6.7d, we see that the late ISW effect completely dominates the SW effect as claimed.

### 6.2.6 Isocurvature $\Lambda$ and Open Models

Isocurvature models differ significantly in that the potentials *grow* until full matter domination. Strong early ISW contributions which are qualitatively similar to the SW term will occur *directly* after recombination and continue until full matter domination (see Fig. 6.1). Thus the projection of scales onto angles will follow a continuous sequence which merges the SW and early ISW ridges (see Fig. 6.10).

For the  $\Lambda$  case, the early ISW effect completely dominates that of the late ISW ef-

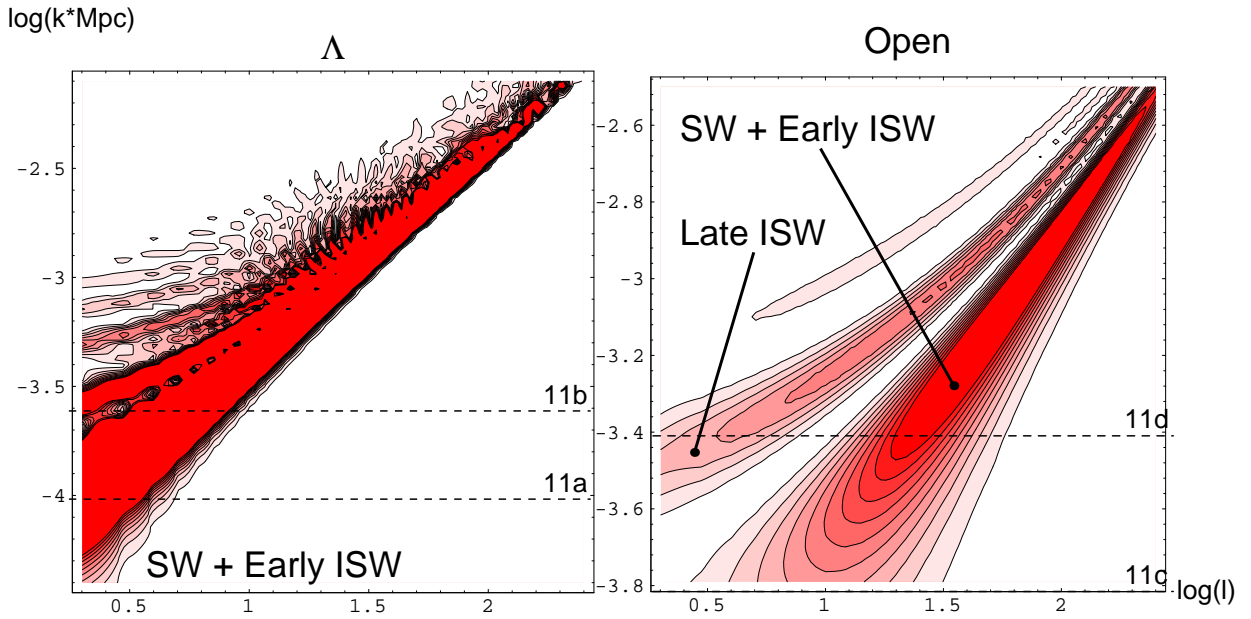


Figure 6.10: Isocurvature Radiation Transfer Function

Unlike their adiabatic counterparts, the potential *grows* in the radiation domination era only to turn over and decay in the curvature and  $\Lambda$  dominated era. The ISW contribution will thus smoothly match onto the SW contribution. This has the effect of merging the SW and ISW ridges to make a wide feature that contributes broadly in  $\ell$ . For  $\Lambda$  models, the early ISW effect completely dominates over the late ISW effect. Scales depicted in Fig. 6.11 are marked here in dashed lines. The model here is  $\Omega_0 = \Omega_b = 0.1$ ,  $h = 0.5$  with standard recombination.

fect. Thus the analytic separation shows that the ISW and SW effects make morphologically similar contributions and the boost in low order multipoles is not manifest. Moreover, the two add coherently creating a greater total effect unlike the adiabatic case (see Fig. 5a,b). Open isocurvature models behave similarly except that the late ISW contributions near its maximum (late ISW ridge) is not entirely negligible. It is thus similar to the adiabatic case (*c.f.* Fig. 6.7d and 6.11d) except that it does not usually dominate the *total* anisotropy. Note that the curvature cutoff can strongly affect the anisotropy spectrum since the curvature scale projects onto  $\ell \simeq 10$  for the SW and early ISW contributions in the  $\Omega_0 = 0.1$  model. There will be a deficit of power at  $\ell \lesssim 10$  if no supercurvature contributions are considered.

On the other hand, the scale invariant model represented here does not present a viable model for structure formation. As discussed in §6.2.2, potential growth leads to an enhancement of large over small scale power. The initially scale invariant isocurvature

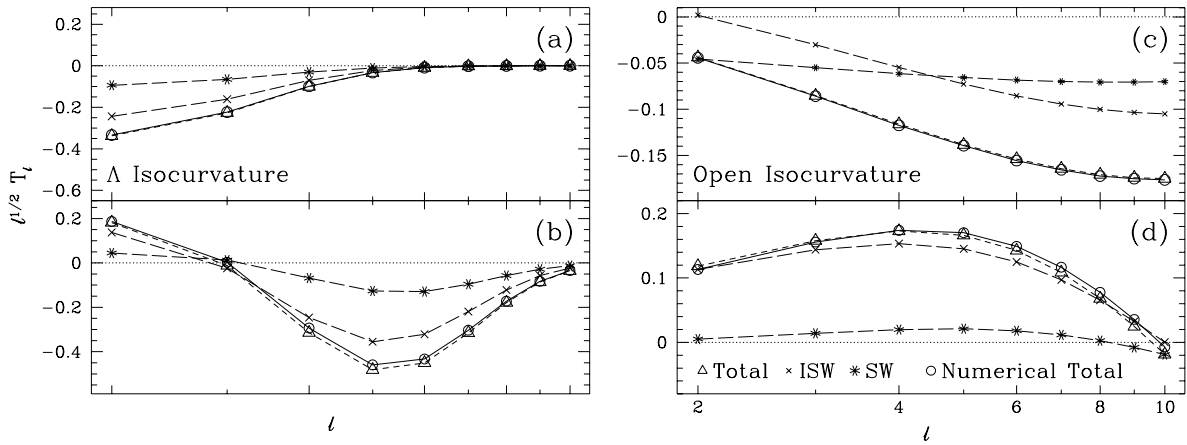


Figure 6.11: Analytic Decomposition: Isocurvature Models

In general, isocurvature models have strong early ISW contributions which mimic and coherently boost the SW effect. Scales are chosen to match the features in Fig. 6.10.  $\Lambda$  models: (a) Notice that the shape of the SW and ISW effects are identical at large scales. (b) Even at the late ISW peak, the early ISW contributions are so strong that the late contributions are never apparent unlike the adiabatic model. Open models: (c) As with  $\Lambda$  models, early ISW and SW contributions are similar in form at large scales. (d) Near the peak of the late ISW contribution however, the relative contributions are similar to the adiabatic case. The model here is  $\Omega_0 = \Omega_b = 0.1$ ,  $h = 0.5$  with standard recombination.

$m = -3$  model has insufficient small scale power to form galaxies. The problem can be alleviated by increasing the spectral index to  $m \simeq -1$ . This has significant effects on the anisotropy. By heavily weighting the small physical scales, we enhance the projection aliasing contribution from the higher ridges of Fig. 6.10. This aliasing or power bleeding from small scales makes the anisotropy spectrum less steep (blue) than the spatial power spectrum (see Fig. 6.12).

In fact, there is an upper limit as to how fast anisotropies can rise with  $\ell$ . Suppose that the spectrum is so blue as to have all contributions come from the smallest physical scale in the problem  $k_{cut}$ , *e.g.* the photon diffusion scale at last scattering. In this case,  $j_\ell(k_{cut}\Delta\eta)$  becomes independent of  $\ell$  and thus  $\Theta_\ell \propto 2\ell + 1$  from equation (6.2) or  $C_\ell \simeq \text{constant}$ . This corresponds to an effective large scale slope of  $n_{\text{eff}} = 3$  as compared with the adiabatic SW prediction of equation (6.13). Isocurvature  $m = -1$  models are an intermediate case with  $n_{\text{eff}} \simeq 2$ . Since the effect is from small scale power aliasing for  $m \gtrsim -2$ , the effective anisotropy slope will only weakly depend on the initial power spectrum slope  $m$ . In Fig. 6.13, we plot the dependence of isocurvature large scale anisotropies with  $m$ . Note that because the power comes from small scales, large scale anisotropies are not sensitive to the initial

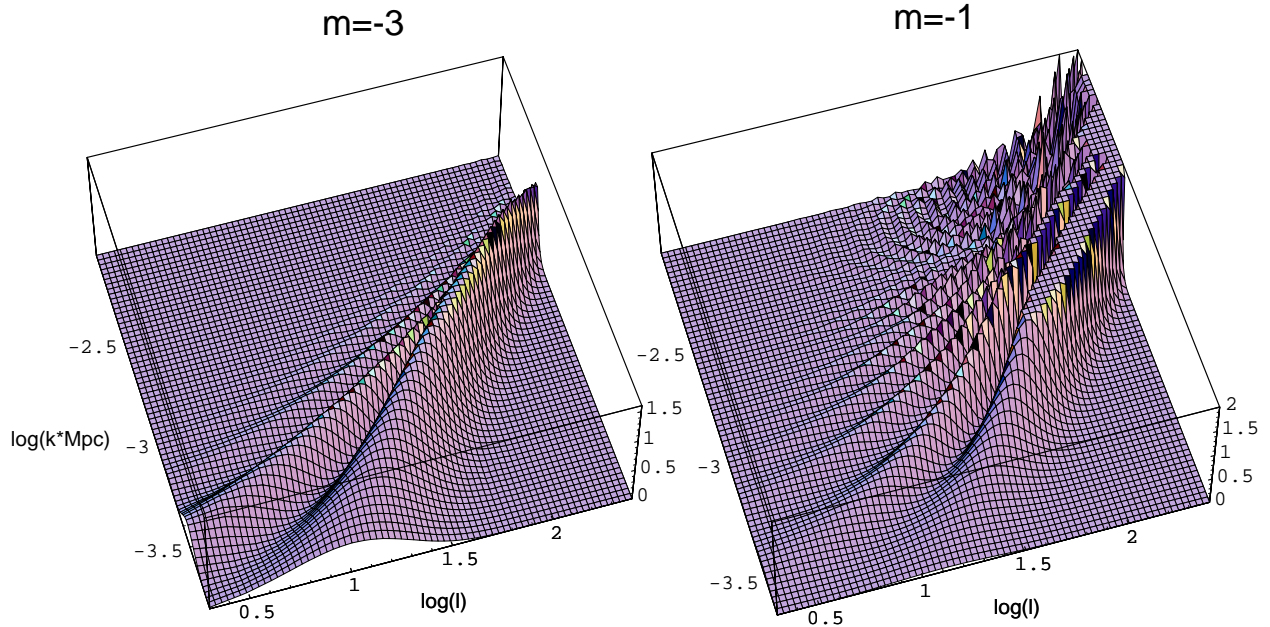


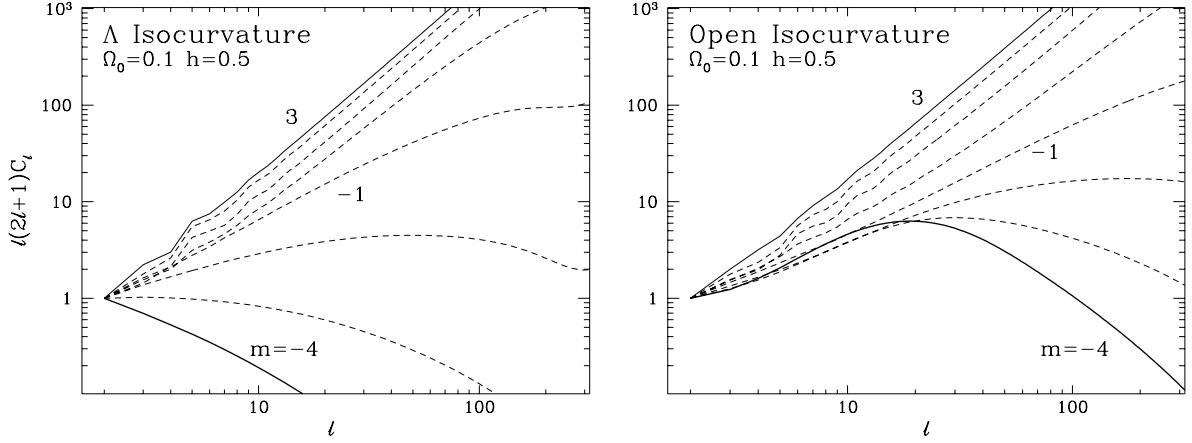
Figure 6.12: Aliasing Effect

The full open isocurvature photon power spectrum for  $k^3|S(0)|^2 \propto k^{m+3}$ . (a) Scale invariant  $m = -3$ . (b) Blue  $m = -1$ . The steeply blue spectrum required by large scale structure constraints suffers projection aliasing. Large scale anisotropies are dominated by small scale power leaking through the projection. The anisotropy spectrum is thus less blue than the spatial power spectrum and insensitive to the large scale power spectrum.

spectrum at large spatial scales. In particular, possible curvature scale ambiguities, such as the absence (or presence) of supercurvature modes which can suppress (enhance) the low order multipoles, have little effect on the result for  $m \gtrsim -2$ .

### 6.3 Acoustic Peaks

On scales below the sound horizon, acoustic oscillations imprint hot and cold spots from regions caught in compression and rarefaction at last scattering. Viewed today, these become peaks in the anisotropy power spectrum. Since acoustic oscillations are generic in the gravitational instability scenario for structure formation, these peaks contain valuable model-independent cosmological information.

Figure 6.13: The  $m$  Dependence of Isocurvature Spectra

Blue spectra  $m \gtrsim -2$  are dominated by small scale power aliased onto large angle anisotropies. The effective slope never exceeds  $n_{\text{eff}} = 3$ . In the  $m \simeq 1$  regime  $n_{\text{eff}} \simeq 2$  for both open and  $\Lambda$  models. Red spectra show different open and  $\Lambda$  models due to the lack of supercurvature modes in the open case which cuts off anisotropies. This is more severe in isocurvature models since the curvature scale at early ISW formation scales projects onto smaller angles than for their adiabatic late ISW counterparts.

### 6.3.1 Mathematical Description

Acoustic contributions are described by the phase and the amplitude of the sound waves at last scattering. Since different  $k$  modes are frozen at different phases of their oscillation, there will in general be a series of peaks in the temperature and velocity spectra at last scattering. The bulk velocity of the photon fluid contributes as a Doppler shift in the observed temperature. The fluctuations captured at last scattering for a scale invariant adiabatic model is displayed in Fig. 6.14.

These fluctuations are projected onto anisotropies as

$$\begin{aligned} \frac{\Theta_\ell(\eta)}{2\ell+1} &= [\Theta_0 + \Psi](\eta_*, k) X_\nu^\ell(\chi - \chi_*) + \Theta_1(\eta_*, k) \frac{1}{k} \frac{d}{d\eta} X_\nu^\ell(\chi - \chi_*) \\ &\quad + \int_{\eta_*}^{\eta} (\dot{\Psi} - \dot{\Phi}) X_\nu^\ell(\chi - \chi') d\eta', \end{aligned} \quad (6.21)$$

(see Appendix A.2.3 for a derivation). The dipole projects in a different manner than the monopole because of its angular dependence. The face on  $\mathbf{k} \perp \boldsymbol{\gamma}$  mode of the “main projection” (see Fig. 6.3 and 1.7) vanishes for the Doppler effect which arises because of the line of sight velocity. This causes velocity contributions to be out of phase with the temperature as the derivative structure suggests and indicates that the two effects add in quadrature.

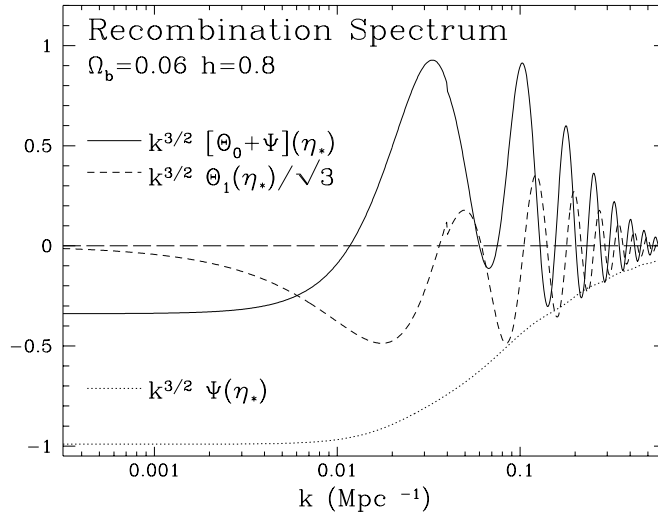


Figure 6.14: Fluctuations at Last Scattering

Analytic separation from Appendix A.2.3. Notice that the dipole is significantly smaller than the monopole as expected but is not negligible, especially near the zeros of the monopole oscillations. In particular, along with the early ISW effect, it fills in fluctuations *before* the first acoustic peak. Due to baryon contributions, gravity is able to shift the equilibrium position of the fluctuations, leading to a modulation of the monopole peaks (see §3.2). We have drawn in the zero level of the oscillations to guide the eye. The kink at  $k = 0.04 \text{ Mpc}^{-1}$  is due to the joining of the large and small scale solutions.

Due to the finite duration of last scattering, the effective fluctuations  $[\Theta_0 + \Psi](\eta_*)$  and  $\Theta_1(\eta_*)$  are more severely diffusion damped than one might naively expect. As the ionization fraction drops due to recombination, the mean free path and hence the diffusion length increases. We will see how this affects the amplitude of oscillations in §6.3.4. Once this is accounted for, the tight coupling description of the acoustic oscillations from §5.2 leads to an excellent description of the resultant anisotropy (see [82] and Appendix A.2.3). It is useful however to extract a few simple model-independent results.

### 6.3.2 Location of the Peaks

The most robust feature of the acoustic oscillations is the angular location of the peaks. Consider first, the spatial power spectrum at last scattering. Peaks will occur at extrema of the oscillations, *i.e.*

$$k_p r_s(\eta_*) = \begin{cases} p\pi & \text{adi} \\ (p - 1/2)\pi, & \text{iso} \end{cases} \quad (6.22)$$

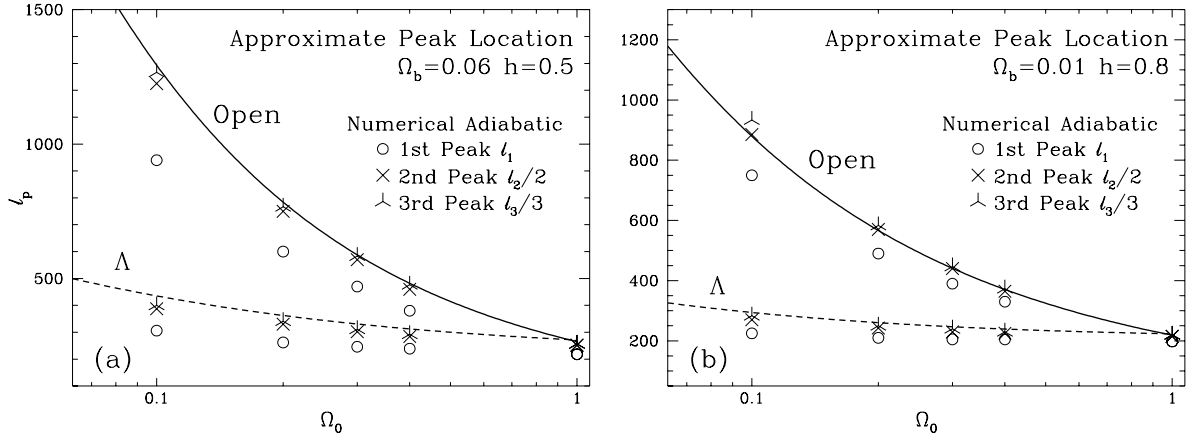


Figure 6.15: Acoustic Peak Location

The physical scale of the peaks is simply related to the sound horizon at last scattering and corresponds to multiples of the angle that this scale subtends on the sky  $\ell_p = p\pi r_\theta / r_s$  for adiabatic models. Varying  $\Omega_0 h^2$  changes both the sound horizon at  $\eta_*$  and the present horizon  $\eta_0$  leaving little effect. For open models, a given scale will correspond to a smaller angle by geodesic deviation. This projection estimate for the peak location is valid for pure acoustic contributions and underestimates the scale of the first peak in low  $\Omega_0 h^2$  models due to neglect of the early ISW effect.

where the sound horizon at last scattering is

$$r_s(\eta_*) = \int_0^{\eta_*} c_s d\eta' = \frac{2}{3} \frac{1}{k_{eq}} \sqrt{\frac{6}{R_{eq}}} \ln \frac{\sqrt{1+R_*} + \sqrt{R_* + R_{eq}}}{1 + \sqrt{R_{eq}}}, \quad (6.23)$$

with  $k_{eq} = (2\Omega_0 H_0^2 a_0 / a_{eq})^{1/2}$ ,  $a_{eq}/a_0 = 2.38 \times 10^{-5} \Theta_{2.7}^4 (\Omega_0 h^2)^{-1} (1 - f_\nu)^{-1}$  and recall  $R = 3\rho_b/4\rho_\gamma$ , *i.e.*

$$\begin{aligned} R_{eq} &= \frac{1}{1 - f_\nu} \frac{3\Omega_b}{4\Omega_0}, \\ R_* &= 31.5\Omega_b h^2 \Theta_{2.7}^{-4} (z_*/10^3)^{-1}, \end{aligned} \quad (6.24)$$

$\Theta_{2.7} = T_0/2.7\text{K}$  and  $(1 - f_\nu)^{-1} = 1.68$  for three massless neutrinos.

From equation (6.15), the scale  $k_p$  subtends an angle

$$\ell_p \simeq k_p r_\theta(\eta_*), \quad (6.25)$$

where

$$r_\theta(\eta_*) \simeq \begin{cases} 2(\Omega_0 H_0)^{-1} & \Omega_\Lambda = 0 \\ 2(\Omega_0 H_0^2)^{-1/2} (1 + \ln \Omega_0^{0.085}). & \Omega_\Lambda + \Omega_0 = 1 \end{cases} \quad (6.26)$$

For low  $\Omega_b h^2$ ,  $R_* \ll 1$  and the sound horizon at last scattering reduces to

$$r_s(\eta_*) \simeq \frac{1}{\sqrt{3}} \eta_* \simeq \frac{2}{\sqrt{3}} (\Omega_0 H_0^2)^{-1/2} [(1 + x_R)^{1/2} - x_R^{1/2}] z_*^{-1/2}, \quad (6.27)$$

where the radiation contribution at last scattering produces the modification factor in square brackets with  $x_R = a_{eq}/a_*$ . Note that the correction factor in equation (6.27) goes asymptotically to 1 and  $\frac{1}{2}x_R^{-1/2} \propto (\Omega_0 h^2)^{1/2}(1-f_\nu)^{1/2}$  in the high and low  $\Omega_0 h^2$  limits respectively.

Let us summarize these results. Adiabatic models will possess peaks in  $\ell$  that follow a series (1 : 2 : 3 : 4...), whereas isocurvature models obey the relation (1 : 3 : 5 : 7...) due to their phase difference (see §5.2.2). The fundamental angular scale on which these series are based is that which is subtended by the sound horizon at last scattering. It is purely dependent on the background dynamics, matter content, and geometry and thus can be used as a robust probe of these fundamental cosmological parameters. The scale is only weakly sensitive to the baryon content if it is near the value required by nucleosynthesis  $\Omega_b h^2 \simeq 10^{-2}$  but becomes increasingly sensitive as  $\Omega_b h^2$  increases beyond the point at which the photon-baryon fluid is baryon dominated at last scattering  $\Omega_b h^2 \gtrsim 0.03$ . The radiation content at last scattering increases the expansion rate and thus decreases the horizon scale at last scattering. If  $\Omega_0 h^2$  is sufficiently low, the location of the peaks can provide an interesting constraint on the matter-radiation ratio, including perhaps the number of relativistic (massless) neutrino species. Otherwise, changes in the age of the universe through  $\Omega_0 h^2$  and  $\Omega_\Lambda$  largely scale out of the ratio between the two scales but may provide some constraint on large  $\Lambda$  models.

The location of the peaks is by far the most sensitive to the presence of curvature in the universe. Curvature makes the sound horizon at last scattering subtend a much smaller angle in the sky than a flat universe. In Fig. 6.15, we compare open and  $\Lambda$  geometric effects. The corresponding spectra are plotted in Figs. 6.6b and 6.9. Notice that aside from the first peak, the numerical results agree quite well with the simple projection scaling. This is because the first peak also obtains contributions from the early ISW effect. Because of its later generation, those contributions subtend a larger angle on the sky. They also are generated when radiation is less important. Thus for example, in an open universe, the angular location scales close to  $\Omega_0^{1/2}$  even in a low  $\Omega_0 h^2$  model.

### 6.3.3 Heights of the Peaks

The heights of the peaks are somewhat more model dependent than their locations since they will be controlled by the initial spectrum of fluctuations. However, for initial conditions that are featureless (*e.g.* the commonly assumed power law models) in the decade

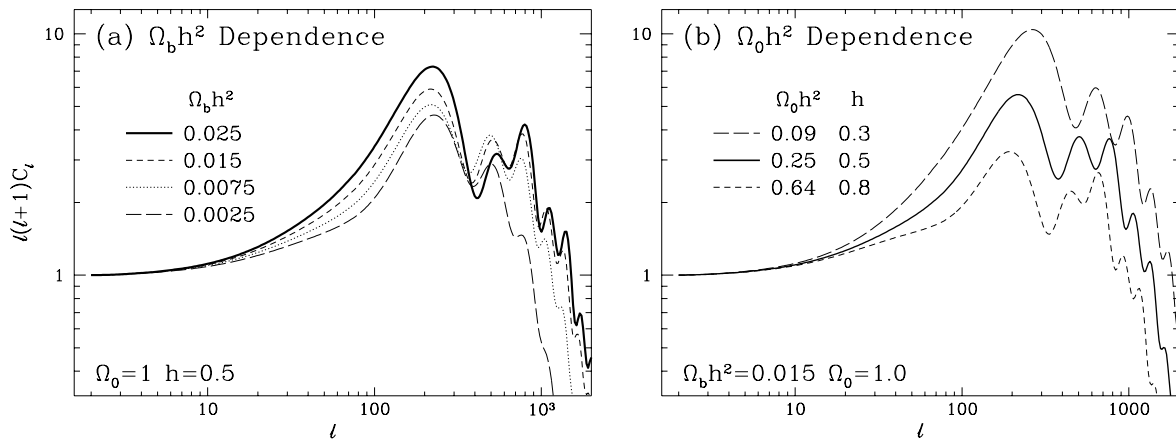


Figure 6.16: Acoustic Peak Heights

(a) The baryon-photon ratio  $R \propto \Omega_b h^2$  determines the balance between pressure and gravity and thus the zero point of the oscillation. Gravitational enhancement of compression leads to higher odd peaks as  $\Omega_b h^2$  increases. For sufficiently high  $\Omega_b h^2$ , the even peaks cannot be distinguished at all. (b) Decay of the potentials  $\Psi$  and  $\Phi$  due to radiation pressure inside the horizon during radiation domination drives the oscillation to higher amplitude. If matter-radiation equality is delayed by lowering  $\Omega_0 h^2$ , this enhancement can boost the first few peaks. The radiation also changes the expansion rate and shifts the location of the peaks.

or so of scales that yield observable peaks, the *relative* heights again contain nearly model independent information.

Aside from the initial spectrum, essentially two quantities control the heights of the peaks: the baryon-photon ratio  $\Omega_b h^2$  and the matter-radiation ratio  $\Omega_0 h^2(1 - f_\nu)$  (see Fig. 6.16). The presence of baryons increases the gravitating mass of the fluid leading to more gravitational compression of the fluid from baryon drag. Thus every other peak will be enhanced by gravitational effects on the baryons. As discussed in §5.2.2, these are the odd peaks for the adiabatic mode and the even for the isocurvature. Enhancement only occurs if the gravitational potential is still significant. In the radiation-dominated epoch, the gravitational potential decays after sound horizon crossing. Thus the alternating series of peaks only occurs for scales that cross after radiation domination leading to a pattern that is dependent on the matter-radiation ratio.

In adiabatic models, the decay of the potentials  $\Psi$  and  $\Phi$  lead to driving effects from infall and dilation. This boosts oscillations by a factor of  $\sim 5$  in amplitude for modes that cross in radiation domination. By delaying equality through lowering  $\Omega_0 h^2(1 - f_\nu)$ , we can bring this effect to larger scales and thus boost more of the peaks. For isocurvature

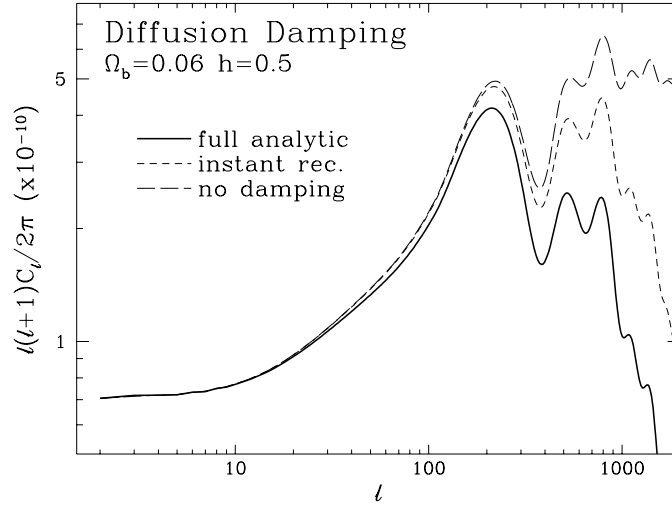


Figure 6.17: Diffusion Damping

The effect of the finite duration of last scattering from the results of Appendix A.2.3. Estimating the damping in the instantaneous recombination approximation leads to a significant underestimate of the damping scale. It is however far better than neglecting diffusion damping entirely.

models, the opposite occurs. By delaying equality, we take away potential growth from larger and larger scales. This lowers the radiation fluctuation.

### 6.3.4 Diffusion Damping at Recombination

At small scales, the features described above for the heights of the peaks can be hidden by diffusion damping. We obtain the diffusion damped fluctuation at last scattering from the acoustic solutions of equation (5.52), denoted by an overhat, with the relations (see Appendix A.3.1 [82])

$$\begin{aligned} [\Theta_0 + \Psi](\eta_*) &= [\hat{\Theta}_0 + \Psi](\eta_*)\mathcal{D}(\eta_*, k), \\ \Theta_1(\eta_*) &= \hat{\Theta}_1(\eta_*)\mathcal{D}(\eta_*, k), \end{aligned} \quad (6.28)$$

where we assume  $R\Psi(\eta_*) \ll \Theta_0$  and the damping factor is weighted by the visibility function

$$\mathcal{D}(\eta_*, k) = \int_0^{\eta_*} d\eta \dot{\tau} e^{-\tau} e^{-(k/k_D)^2}. \quad (6.29)$$

with the damping scale  $k_D(\eta)$  calculated from equation (5.59). Since the visibility function  $\dot{\tau}e^{-\tau}$  goes to a delta function for large  $\tau$ , this definition also coincides with its tight-coupling

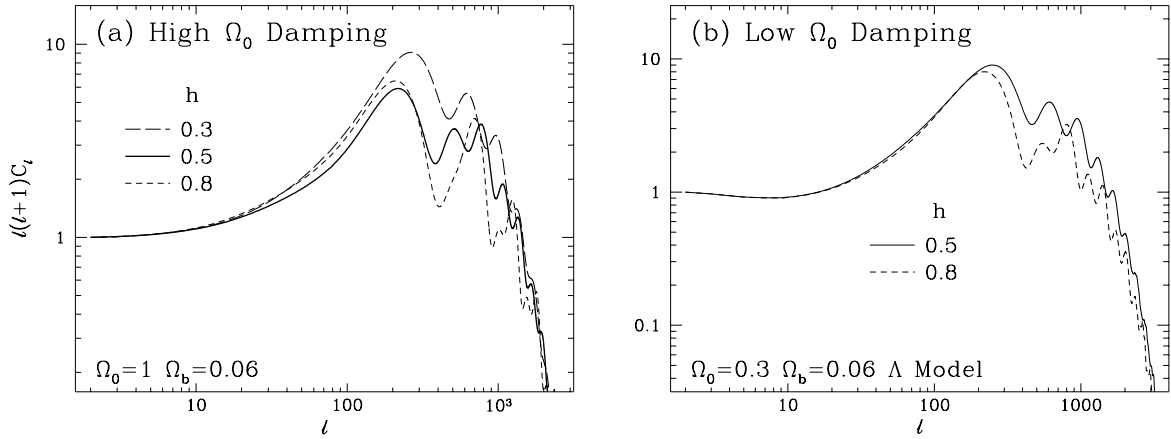


Figure 6.18: Damping Scale

The diffusion damping scale depends somewhat differently on cosmological parameters than the acoustic scale. It is more sensitive to  $\Omega_b$  (see Fig. 6.16) and less sensitive to  $h$ . Its presence can also alter the pattern of heights expected from the acoustic peaks, *e.g.* the small scale boost from dilation and the alternating peak heights from infall.

definition from equation (5.58). Note that the ionization history enters in two places: the increase in the diffusion length  $k_D^{-1}$  and the visibility function weighting. Since the visibility function peaks at  $z \simeq 10^3$  nearly independent of cosmological parameters and is by definition normalized to have unit area, much of the qualitative behavior of the damping can be determined by examining  $k_D^{-1}$ .

Recall from §5.2.3 that the diffusion length is approximately the distance a photon can random walk by  $\eta_*$ ,  $k_D^{-1} \propto \sqrt{\eta_* \lambda_C}$ , where the Compton mean free path is  $\lambda_C \propto (x_e n_b)^{-1}$ . The behavior of the diffusion length through last scattering will be determined by the evolution of the ionization fraction. In Appendix A.2.3, we will show how to construct the diffusion length from a realistic treatment of recombination. However, to obtain simple scaling results, the Saha approximation for the equilibrium ionization suffices.

The Saha equation assumes that photoionization and recombination of hydrogen  $e + p \leftrightarrow H + \gamma$  are in equilibrium. If the photon chemical potential is vanishingly small as required by the FIRAS observation [116], the chemical potentials of the other species must satisfy  $\mu_e + \mu_p = \mu_H$ . The number density of a non-relativistic species  $x$  is given by

$$n_x = g_x \left( \frac{m_x T_x}{2\pi} \right)^{3/2} e^{(\mu_x - m_x)/T_x} \quad (6.30)$$

where  $g_x$  is the spin multiplicity. This chemical potential relation then implies the Saha

equation

$$\frac{n_e n_p}{n_H n_b} = \frac{x_e^2}{1 - x_e} = \frac{1}{n_b} \left( \frac{m_e T}{2\pi} \right)^{3/2} e^{-(m_e + m_p - m_H)/T} \quad (6.31)$$

where we neglect the helium fraction,  $n_b = n_p + n_H$  and the strong thermal coupling between photons, electrons, and baryons at last scattering has allowed us to set all the temperatures equal (see §3.1.2). Note that  $m_e + m_p - m_H = 13.6\text{eV}$ , the electron binding energy.

The interesting result here is that as the ionization drops to zero, its parameter dependence goes to  $x_e \propto (\Omega_b h^2)^{-1/2}$  at fixed redshift (or temperature). The final damping length approximately scales as  $k_D^{-1}(\eta_*) \propto \eta_*^{1/2} (\Omega_b h^2)^{-1/4}$ . The damping angular scale therefore becomes

$$\ell_D \propto \eta_*^{-1/2} (\Omega_b h^2)^{1/4} r_\theta(\eta_*) \quad (6.32)$$

At asymptotically high and low  $\Omega_0 h^2$ , this goes to  $\Omega_0^{-3/4} \Omega_b^{1/4}$  and  $\Omega_0^{-5/4} \Omega_b^{1/4} h^{-1/2}$  in an open universe and  $\Omega_0^{-1/4} \Omega_b^{1/4}$  and  $\Omega_0^{-1/2} \Omega_b^{1/4} h^{-1/2}$  in a  $\Lambda$  universe. The damping scale is thus somewhat more strongly dependent on  $\Omega_b$  than the acoustic scale but even more weakly dependent on  $h$  alone (see Fig. 6.18). The Saha prediction requires modification for high  $\Omega_b h^2$  models due to the increasing importance of the Lyman- $\alpha$  opacity at last scattering [84].